

Thin-finger growth and droplet pinch-off in miscible and immiscible displacements in a periodic network of microfluidic channels

Agnieszka Budek,^{1,2} Piotr Garstecki,³ Adam Samborski,³
 and Piotr Szymczak^{1,a)}

¹*Institute of Theoretical Physics, Faculty of Physics, University of Warsaw, Pasteura 5,
 02-093 Warsaw, Poland*

²*Institute of Geophysics, Polish Academy of Sciences, Ksiecia Janusza 64,
 01-452 Warsaw, Poland*

³*Institute of Physical Chemistry, Polish Academy of Sciences, Kasprzaka 44/52,
 01-224 Warsaw, Poland*

(Received 16 December 2014; accepted 23 October 2015; published online 18 November 2015)

We report the results of experimental and numerical studies of two-phase flow in a periodic, rectangular network of microfluidic channels. This geometry promotes the formation of anisotropic, dendrite-like structures during viscous fingering experiments. The dendrites then compete with each other for the available flow, which leads to the appearance of hierarchical growth pattern. Combining experiments and numerical simulations, we analyze different growth regimes in such a system, depending on the network geometry and fluid properties. For immiscible fluids, a high degree of screening is present which results in a power-law distribution of finger lengths. Contrastingly, for miscible fluids, strong lateral currents of displaced fluid lead to the detachment of the heads of the longest fingers from their roots, thus preventing their further growth. © 2015 AIP Publishing LLC. [<http://dx.doi.org/10.1063/1.4935225>]

I. INTRODUCTION

The unstable infiltration of a more viscous fluid by a less viscous one, termed viscous fingering, is one of the better studied pattern forming phenomena, remaining a topic of active research since its discovery by Hill.¹ A classical setup to study this process is a Hele-Shaw cell of either radial or rectangular form,²⁻⁴ but the phenomenon was also studied in porous media, with a number of important differences between the two cases.⁵ In the Hele-Shaw cell, the instability leads to the emergence of smooth fingers, with a characteristic length, R_0 , defined by an interplay of capillary and viscous forces,⁶ $R_0 \sim b/\sqrt{Ca}$, where b is the cell thickness and the capillary number $Ca = \mu V/\sigma$ (with μ the displaced fluid viscosity, V the velocity, and σ the surface tension). This length scale characterizes the initial destabilization of the interface, later however the pattern coarsens until (in rectangular geometry) eventually a single finger emerges with a characteristic width comparable with that of the system. In radial geometry, the many-fingered pattern persists, forming new fingers by successive tip-splitting.

On the other hand, if the process takes place in a porous medium, the radius of curvature of the interface is limited by the characteristic pore radius, R_p , which is usually orders of magnitude smaller than the system size. If the displaced fluid preferentially wets the solid matrix, then the resulting structures are ramified fractals,^{7,8} with the randomness amplified by the quenched disorder in the distribution of pore radii. On the other hand, if the displacing fluid preferentially wets the matrix, then the width of emerging fingers is much larger than the characteristic pore size, and depends on the flow rate, surface tension, and medium permeability.⁷

a) piotr.szymczak@fuw.edu.pl

It is of interest to explore the intermediate case in which this source of randomness is eliminated by considering viscous fingering in periodic network of channels. The insights from theoretical lattice models of fractal growth^{9,10} and experimental studies^{11–14} suggest that in such case lattice anisotropy effects become important. This can have a strong impact on resulting structures: as we show below, in rectangular systems, in a broad range of lattice geometries orientation of the pressure gradient along the lattice direction promotes the growth of long and thin dendrites (“thin fingers”). The fingers then compete with each other for the available flow, which leads to the appearance of hierarchical growth pattern.

This is the regime that we are particularly interested in, for a variety of reasons. First, a simple, linear geometry of the fingers together with the fact that their growth is to a large extent deterministic (see Sec. IV), makes such a system particularly attractive from a theoretical point view: one can look upon it as a collection of zero-pressure lines, extending in length only, and interacting through the Laplacian pressure field. An analytical approach to this problem, with use of deterministic Loewner equation^{15,16} has been explored in Refs. 17 and 18. Second, there are several related systems where “long-and-thin” fingers emerge, such as the dendritic growth in some of the electrochemical deposition experiments,^{10,19} wormhole formation in dissolving rocks,²⁰ smoldering combustion,^{21,22} side-branches growth in crystallization,^{23,24} or the evolution of seepage channel networks.^{25,26} Hence, the insight gained from the analysis of the finger growth in the present case might also shed light on the dynamics of these systems.

The present paper studies the viscous fingering in a rectangular, periodic network of microfluidic channels with two goals in mind. The first is to establish under which experimental conditions the “long-and-thin” finger regime can be observed in the rectangular network of microfluidic channels, both in terms of the network characteristics as well as the miscibility of the fluids. The second is to analyze the growth of the fingers and the competition between them: since the pressure gradients at the tips of longer fingers are larger than those over the shorter ones, the former continue to grow, focusing an ever-increasing portion of the flow, at the expense of the latter. For immiscible fluids, this leads to the appearance of a hierarchical, scale-free growth pattern, analyzed in Sec. V. Surprisingly, the miscible case turns out to be different, with the competition between the fingers strongly hindered due to the strong lateral currents of the displaced fluid, which eventually cut off the head of the finger, thus preventing its further growth. The heads continue to move through the system, preserving their shapes, thus forming the “miscible drops.” A detailed analysis of this phenomenon is presented in Sec. VI.

The experiments are supplemented by numerical modeling (Sec. III), which allows us to explore a larger parameter space of different lattice geometries. For the immiscible case, the simulations follow a well-established numerical scheme,^{27,28} which essentially corresponds to using the Hagen-Poiseuille law for all pores and solving the resulting system of equations. In the miscible case, however, such an approach fails to represent the pattern in the correct way. For a proper description of the pattern formation in this case, we propose an extension of the network model, allowing for a layered, parallel flow of both fluids within a single pore. In the thin-finger regime, the simulations show a remarkable agreement with the experimental data on the finger evolution, which is again a reflection of the deterministic character of the dynamics.

II. EXPERIMENTAL SETUP

Studies of micro-models of porous media made of transparent materials such as plastic or glass have yielded much insight into the physics of porous flow.^{8,29–41} Most of these models have a certain amount of randomness introduced into the structure: either by using disordered, packed glass beads or capillaries of variable diameter, which makes the viscous fingers created in that way fractal, ramified patterns. However, some of the models have used regular, periodic pore structures, either by etching a periodic pattern on one of the sides of the Hele-Shaw cell or by performing the infiltration experiments in a regular network of transparent capillary ducts.^{11–14} These experiments have shown a strong impact of the underlying lattice on the patterns—the fingering was dendritic in character with the growth along the lattice directions. However, these experiments were performed

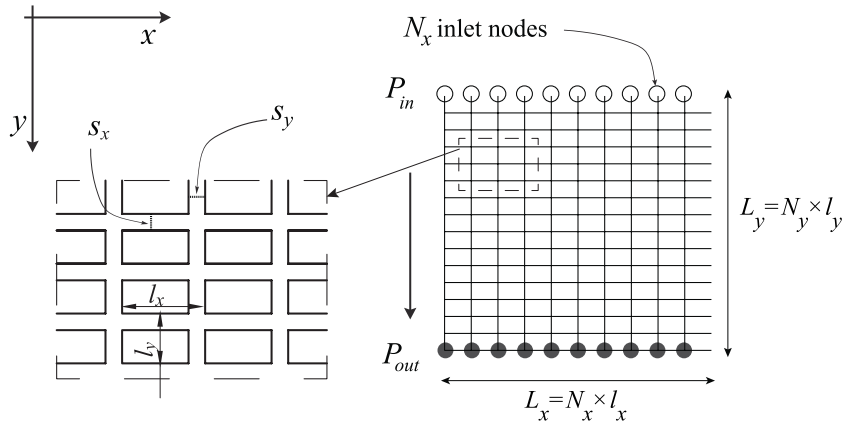


FIG. 1. Schematic view of a rectangular network of channels. The fluid is injected along upper surface where constant pressure is imposed. Geometry of the system is characterized by the ratio of length of transverse to the longitudinal channels, $D = l_x/l_y$, and the corresponding ratio of cross sections, $S = s_x/s_y$.

in a radial geometry, which makes the analysis of channel-channel interaction and competition less straightforward, since the effective distance between radially growing fingers increases in time. Instead, here we focus on the rectangular geometry, where the fingers are forced to grow side by side, which results in a strong competition between them. To our knowledge, the only other study where viscous fingering was analyzed in a perfectly periodic system in rectangular geometry are the works by De Malsche *et al.*⁴² on the fingering in the system of micropillar array columns. However, the geometrical characteristics of that system promoted the formation of just a few wide fingers, spanning many lattice sites, similar to the “thick-finger” regime observed in some of our experiments (see below). The “long-and-thin” finger regime has thus not been explored there.

In recent years, an increasing amount of experiments on drainage and imbibition are performed using microfluidic micro-models.^{41,43,44} Here, we follow a similar approach. The microchannel network has been engraved in the Makroclear® polycarbonate plate using MSG4025 CNC micro milling machine and then bonded with another, flat plate in a thermal press. The details of the bonding procedure are given in Ref. 45.

A schematic view of the channel networks used in this work is presented in Fig. 1. Each network comprises $N_x \times N_y$ nodes, connected with channels. The lengths of transverse and longitudinal channels are denoted by l_x and l_y , whereas $L_x = N_x \times l_x$ and $L_y = N_y \times l_y$ are the total lengths of the system in the x and y direction, respectively.

Two different systems were used in the experiments, with different lengths.

- Plate no. 1: 42×100 channels with $l_x = 1200 \mu\text{m}$ and $l_y = 400 \mu\text{m}$ with the cross sections of $200 \mu\text{m} \times 200 \mu\text{m}$.
- Plate no. 2: 57×26 channels with $l_x = 800 \mu\text{m}$ and $l_y = 1600 \mu\text{m}$ with the cross sections of $400 \mu\text{m} \times 400 \mu\text{m}$.

It is convenient to introduce the dimensionless parameter $D = l_x/l_y$, the ratio of the lengths of transverse and longitudinal channels. The experimental plates correspond then to $D = 3$ (plate 1) and $D = 1/2$ (plate 2). The size of each plate is $6.5 \text{ cm} \times 6.5 \text{ cm}$, of which the part containing channels takes up $5.0 \text{ cm} \times 4.0 \text{ cm}$ (plate 1) and $4.6 \text{ cm} \times 4.2 \text{ cm}$ (plate 2). Additionally, as shown in Fig. 2, the upstream part of each plate is milled to accommodate $5.5 \text{ cm} \times 0.5 \text{ cm} \times 0.25 \text{ cm}$ input reservoir space. The downstream part was milled to accommodate a hierarchical system of outlet channels, which helps in keeping the uniform pressure along the downstream edge of the network. The outlet channels merge into an outlet tube with a tap. The other end of this tube is connected to the pressure control tank, in which a low pressure is maintained by means of a vacuum pump (V-700, Büchi, Switzerland).

During each experiment, the network is initially filled with a viscous fluid, either the motor oil (of $\mu \approx 500 \times 10^{-3} \text{ Pa s}$) or glycerol-water mixture ($\mu \approx 100 \times 10^{-3} \text{ Pa s}$). The invading fluid

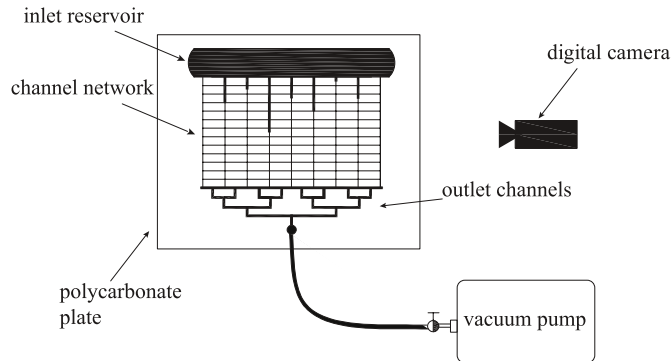
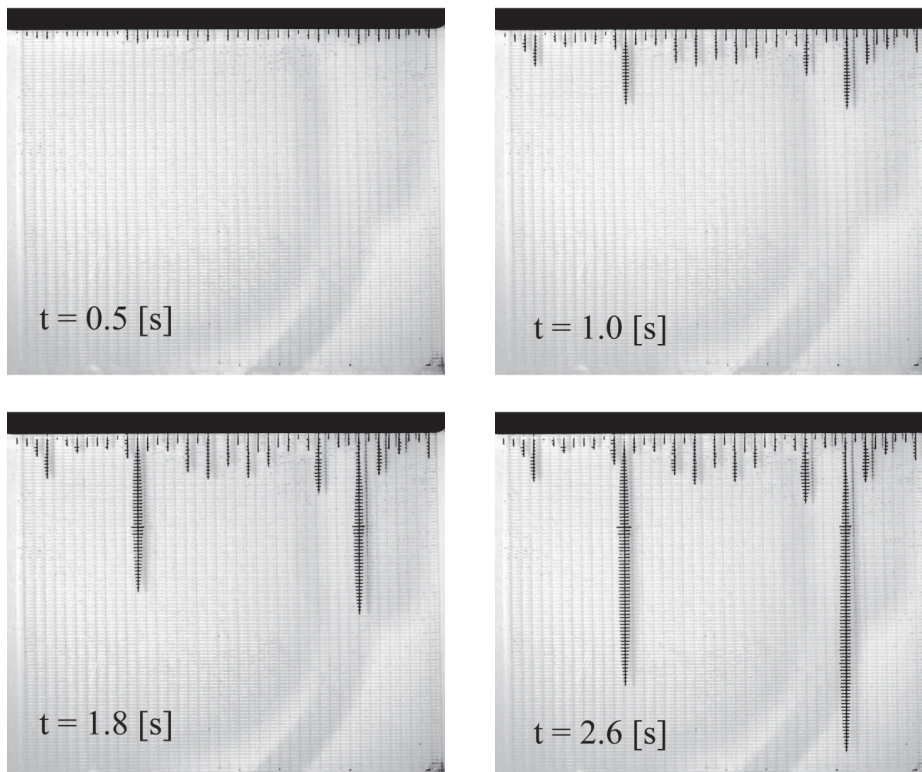


FIG. 2. Schematic representation of the experimental setup.

was water dyed with ink. Note that on the polycarbonate surfaces both glycerol and mineral oil are wetting with respect to water. The mean velocity of fluids in tubes was around 14×10^{-3} m/s. The interfacial tension between water and oil was assumed to be around 15×10^{-3} N/m which corresponds to the capillary number $Ca \approx 0.5$. The mutual diffusion coefficient for water and glycerol is assumed to be 10^{-9} m² s⁻¹, which gives the Péclet number $Pe \approx 10^4$.

The typical experimental results for immiscible viscous fingering (oil and water) are shown in Figs. 3 and 4. The most pronounced features of the experimental patterns are the following.

1. A strong dependence on the lengths of transverse channels. For relatively short connecting channels (Fig. 4) thick fingers are formed, spanning many parallel channels. On the other hand, for longer channels (Fig. 3) long-and-thin-fingers are formed, involving essentially a single longitudinal channel.
2. Characteristic corrugations along the sides of the thick fingers in Fig. 4.

FIG. 3. Experimental patterns for immiscible viscous fingering (water infiltrating oil) for plate no. 1 ($D = 3$).

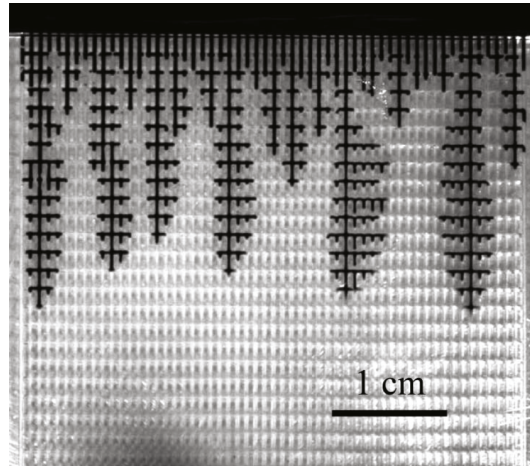


FIG. 4. Experimental patterns for immiscible viscous fingering (water infiltrating oil) for plate no. 2 ($D = 1/2$).

3. A hierarchical finger pattern in Fig. 3, developing in time. Many short fingers are observed, but the growth of most of them is soon stopped and only a few continue to grow. The selection process then repeats itself which results in a distance between the active fingers increasing in time.

For comparison, the miscible fingering results (for glycerol and water) are presented in Figs. 5 and 6. Some of the features of these patterns are similar to what is observed for immiscible fingering—the thickness of the structures increases with decreasing D leading to the appearance of thick fingers at $D = 1/2$. The form of these fingers (Fig. 6) is, however, more smooth than their

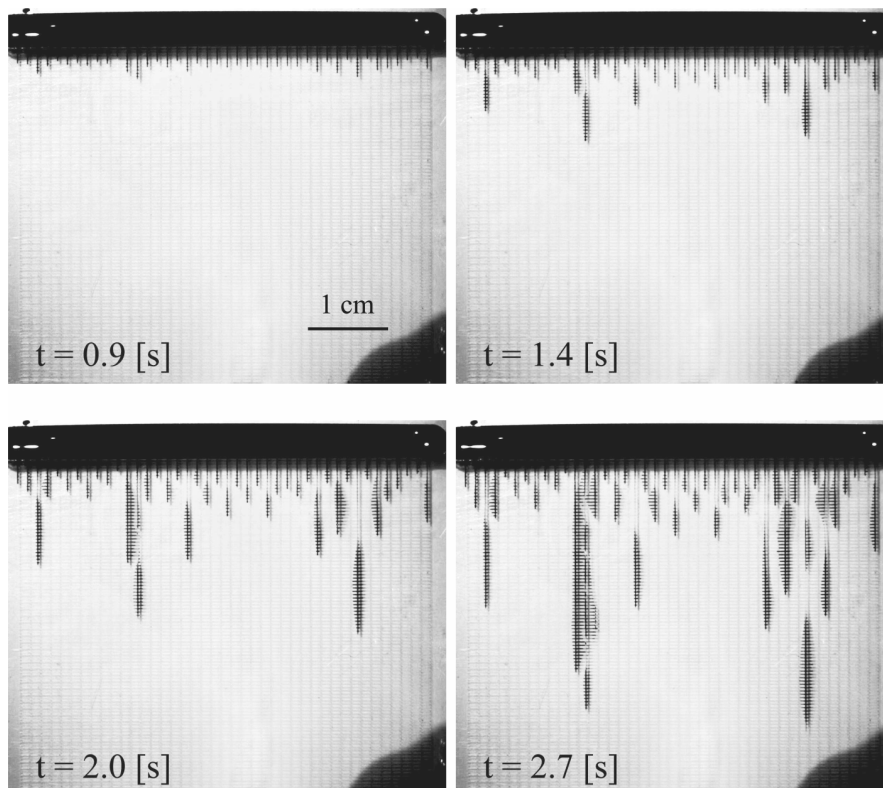


FIG. 5. Experimental patterns for miscible viscous fingering (water infiltrating glycerol) for plate no. 1 ($D = 3$).

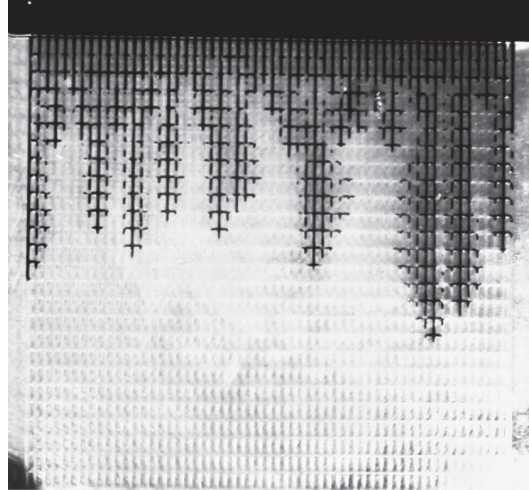


FIG. 6. Experimental patterns for miscible viscous fingering (water infiltrating glycerol) for plate no. 2 ($D = 1/2$).

counterparts in Fig. 4 since there is no surface tension preventing the water from entering the side channels. Another notable feature, pronounced in Fig. 5, is that the heads of the thin fingers in plate 1 in the course of the evolution become disconnected from their bodies. As a result, spear-like “miscible drops” are formed which then continue to move downstream, preserving their shape. This phenomenon is analyzed in more detail in Sec. VI.

III. NUMERICAL MODEL

In order to get a better insight into the pattern formation mechanism, we supplement the experimental study with the numerical simulation using a network model. The basic assumption in the model is that the fluid flow in each elementary channel is governed by the Hagen-Poiseuille equation,

$$q_{ij} = -\frac{\pi}{8\mu l_{ij}} r_{ij}^4 \Delta p_{ij}, \quad (1)$$

where $\Delta p_{ij} = (p_j - p_i)$ denotes pressure drop along the channel joining node i with node j , q_{ij} is the volumetric flux in this channel, l_{ij} and s_{ij} its length and cross-sectional area, respectively. Combining the above with the continuity condition,

$$\sum_i q_{ij} = 0, \quad (2)$$

allows one to find the pressures and flows in the network for single phase flow. Note that in the above we neglect the pressure drops associated with the nodes themselves. When there are two phases, we need to take into account their relative saturations in each channel as well as the surface tension effects on the interface. Here the algorithm differs depending on whether we deal with immiscible or miscible fluids.

A. Immiscible model

In the immiscible case, the two fluids in the channel are separated by a meniscus and the water finger displaces oil almost completely, in a piston-like manner.^{13,46} Importantly, upon entering the intersection, the water finger divides and infiltrates all the side channels, as illustrated in Fig. 7. In the numerical model, we mimic this behaviour by assuming that the invading fluid fills uniformly a given portion of the channel (of length $l_{ij}^{(1)}$), whereas the rest of the channel (i.e., $l_{ij}^{(2)} = l_{ij} - l_{ij}^{(1)}$) is

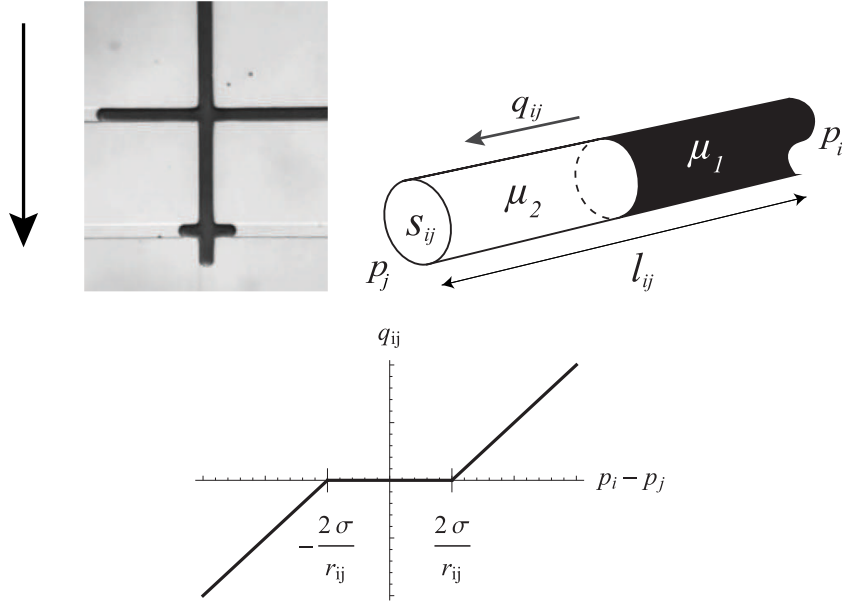


FIG. 7. Piston-like movement of the fluid-fluid interface in an immiscible case: the experiment (left) and a numerical model (right). Pressure-flow relationship in a channel containing an interface (bottom).

filled with the displaced fluid. The volumetric flow in the channel is then given by

$$q_{ij} = \pm \frac{\pi}{8} \frac{1}{\mu_1 l_{ij}^{(1)} + \mu_2 (l_{ij} - l_{ij}^{(1)})} r_{ij}^4 \text{Max}[|p_j - p_i| - \frac{2\sigma}{r_{ij}}, 0], \quad (3)$$

where the indices 1 and 2 are used to denote the invading and displaced fluid, σ is the interfacial tension between the fluids, and the sign depends on the direction of the pressure drop. When the pressure drop is smaller than the capillary pressure, $\frac{2\sigma}{r_{ij}}$, the fluid does not flow, which introduces a nonlinear, diode-like behavior in the flow vs. pressure relationship, as illustrated in Fig. 7. The resulting system of equations is then solved iteratively for pressure values at all nodes.

B. Miscible model

As noted in Ref. 46, the above scheme, although remarkably accurate in reproducing the immiscible displacement in the network, fails to reproduce the miscible fingering patterns. The main reason for this discrepancy is the fact that the infiltration of the miscible fluid into the capillary is non-uniform:^{13,46–48} the invading fluid stays preferentially near the center of the channel, whereas a thick layer of the slower displaced fluid is left behind near the walls. The presence of this layer gives rise to a different behaviour of the fluids at the nodes: as shown in the upper panel of Fig. 8, the invading fluid enters only the channel downstream from the first intersection, whereas the two side channels are bypassed and remain filled with the displaced fluid. After passing the first intersection, the invading fluid filament becomes wider, filling almost the entire channel. As a result, at the next intersection, all the three channels are invaded.

The parallel flow of two phases in the channel can be modelled by a “double Poiseuille” velocity profile, connected through velocity and stress continuity conditions on the interface between the fluids, as shown in Fig. 8. The volume fluxes of both fluids are then given by

$$q_{ij}^{(1)} = - \frac{\pi (r_{ij}^{(1)})^2 (\mu_2 (r_{ij}^{(1)})^2 + 2\mu_1 (r_{ij}^2 - (r_{ij}^{(1)})^2))}{8l_{ij}\mu_1\mu_2} \Delta p_{ij} \quad (4)$$

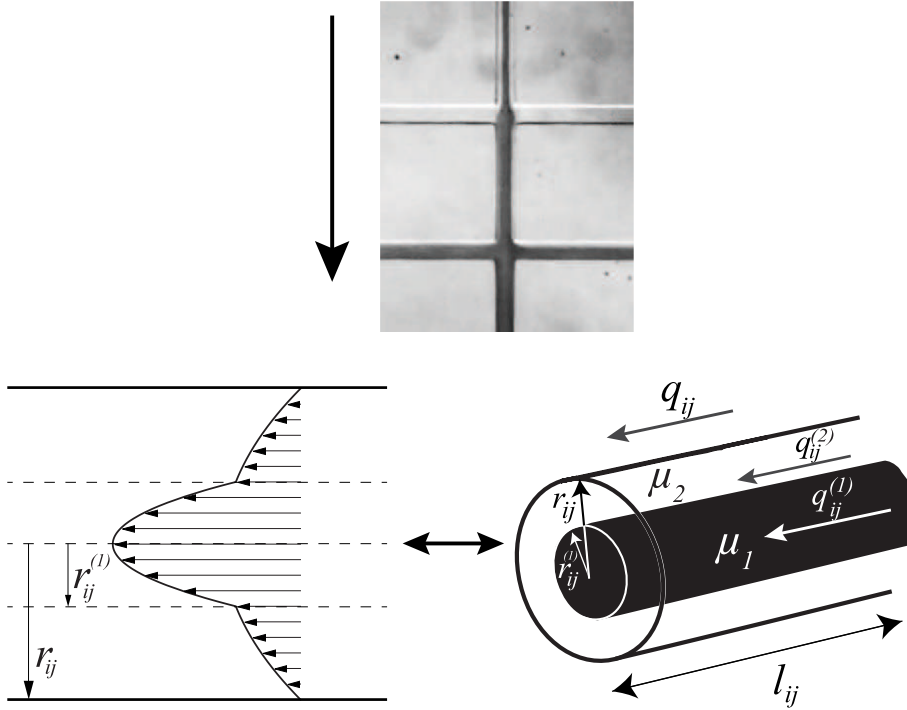


FIG. 8. Schematic of miscible displacement in a capillary tube: the invading fluid occupies the column at the center of the capillary, whereas the displaced fluid forms the annular fluid layer left behind on the tube wall (below, right). The velocity profiles within and around the intruding finger (below, left) and the experimental behaviour of the invading fluid at the successive crossings (above).

and

$$q_{ij}^{(2)} = -\frac{\pi(r_{ij}^2 - (r_{ij}^{(1)})^2)^2}{8l_{ij}\mu_2}\Delta p_{ij}, \quad (5)$$

where $r_{ij}^{(1)}$ is the radius of the cylindrical core filled with the invading fluid. The total flow is then given by

$$q_{ij} = -\frac{\pi((r_{ij}^{(1)})^4(\mu_2 - \mu_1) + \mu_1 r_{ij}^4)}{8l_{ij}\mu_1\mu_2}\Delta p_{ij}. \quad (6)$$

Finally, in the case when the invading fluid does not fill the entire length of a channel,

$$q_{ij} = -\left(\frac{8l_{ij}^{(1)}\mu_1\mu_2}{\pi((r_{ij}^{(1)})^4(\mu_2 - \mu_1) + \mu_1 r_{ij}^4)} + \frac{8\mu_2(l_{ij} - l_{ij}^{(1)})}{\pi r_{ij}^4}\right)^{-1}\Delta p_{ij}, \quad (7)$$

where, as before, $l_{ij}^{(1)}$ denotes the length of a channel occupied by the invading fluid.

C. Implementation of the model

The above-described model is implemented numerically in the following way:

- At the beginning of the simulation the positions of the front in the first (inlet) row of the channels are randomly chosen from a uniform distribution: $l_{ij}^{(1)} \in [0, l_{ij}]$. Additionally, in the miscible case, the radius of the invading core is set to $r_{ij}^{(1)} = 0.7r_{ij}$ in the first row of channels (inlet channels). This corresponds to the assumption that about 50% of the incoming volume is taken up by displacing liquid, which holds at large flow rates.⁴⁷ In all the other channels

(except for the first row), the length and radius of the invading core are set to zero. No significant change in the resulting patterns has been observed when varying the initial value of $r_{ij}^{(1)}$ in the inlet channels between $0.5r_{ij}$ and $0.95r_{ij}$.

- In each time step, the pressures and flows in the network are obtained by solving (2) together with (3) for immiscible fluids or (4)-(7) for miscible ones. Multifrontal Massively Parallel Solver (MUMPS)^{49,50} is used to invert the resulting sparse matrices. Due to the nonlinear character of pressure-flow (Eq. (3)), an iterative method must be used to obtain the pressure field for immiscible fluids. Nonlinear terms for the first iteration in a time step are based on pressure values from the previous time step and the iterations are continued until a self-consistent solution is found.
- A new position of the interface (new value of $l_{ij}^{(1)}$ and $r_{ij}^{(1)}$) is being determined:
 - (i) For immiscible fluids, the velocity of the interface is taken to be the mean velocity of the fluid in a given channel, i.e., $q_{ij}/\pi r_{ij}^2$. Therefore, in channels occupied by both fluids, the length of invading fluid, $l_{ij}^{(1)}$, increases by $\Delta t q_{ij}/\pi r_{ij}^2$, over the time step Δt , until it reaches l_{ij} . At intersections, the invading fluid is divided according to the total volume flux through each branch, however, it can enter a new channel only if pressure drop in it is larger than the capillary term.
 - (ii) In the miscible case, we assume that the fluid interface moves accordingly to the mean velocity of the invading fluid, $q_{ij}^{(1)}/\pi r_{ij}^{(1)2}$, calculated according to Eq. (4). The radii of the cylindrical cores of the invading fluid, $r_{ij}^{(1)}$, are updated in each time step based on the volumes of each fluid flowing in and out of a given channel. When the invading fluid enters the intersection, it is first directed downstream (to the continuation of the inlet conduit). However, if the incoming volume of the invading fluid is larger than the volume which can be transported by the downstream channel, then the surplus volume is directed to the side channels.
- The simulation terminates when the invading fluid reaches the outlet of the system.

Although formulae (1)-(7) are given specifically for the case of cylindrical capillaries, the overall structure of the model will remain the same for other cross-sectional geometries. In the experiments, the capillaries are square in cross section, which would affect the numerical coefficient in Eq. (1)⁵¹ and the shape of the intruding fluid column in Fig. 8. A detailed account of those effects is possible but not practical, given that other more severe approximations are being made in the model (e.g., the assumption that there are no pressure drops in the intersections).

IV. NUMERICAL RESULTS

The simulations were performed on rectangular networks designed in analogy to the ones used in the experiment. In this case, however, we allow the transverse and longitudinal channels to differ not only in length, but also in the cross-sectional area. The networks are thus characterized by both $D = l_x/l_y$ and another parameter, $S = s_x/s_y$, the ratio of the cross-section areas. We set constant pressure drop between inlet and outlet. The viscosity ratios were set to 500 (in immiscible case) or 100 (in miscible case), and the capillary number was fixed at $Ca = 0.5$, matching the experiment.

To validate the numerical model, we compare the simulated and experimental evolution of the fingers for the same initial positions of the water-oil interface corresponding to the first frame in Fig. 3. Fig. 9 shows the numerical results obtained in such a setup. The invaded regions are marked in black, whereas the displaced fluid is assumed to be transparent. Both the capillary number and the viscosity ratio correspond to the experimental conditions. The simulation was initialized with the geometry read off from the experimental data corresponding to the early stage of the evolution, when the fingers reach the height of a few l_y only (first panel on the left in Fig. 9).

Given the approximate nature of the model, it is hard to relate the computational time and the physical time in the experiment, thus a fitting parameter was used here, by matching the initial slope of the finger length dependence on time. The numerical data compare favourably with the

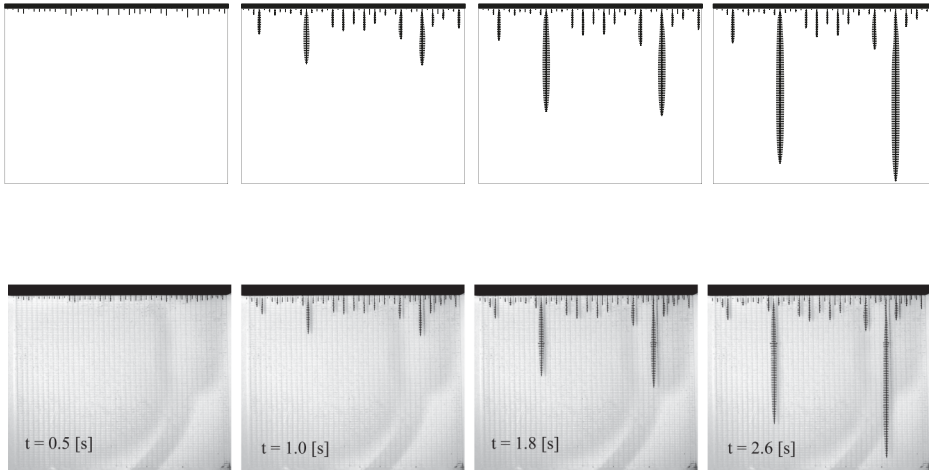


FIG. 9. Simulation with immiscible fluids for $D = 3$ and $S = 1$ compared with experiment (bottom). The initial front between the fluids in the simulation has been set as the one obtained in the experiment (frame one, $t = 0.5$ s). Both the capillary number and the viscosity ratio correspond to the experimental conditions.

experimental evolution in Fig. 3—not only a general, hierarchical structure of the channels is faithfully reproduced, but even the lengths of individual fingers are in a very good agreement between the simulation and experiment. This shows that, except for the initial, noise-driven stage of the evolution, which results in the appearance of the finger seeds (which are then loaded into the simulation as the initial geometry), the dynamics is largely deterministic, driven by a strong competition between the fingers for the available flow. Such a deterministic dynamics of the fingers is a characteristic feature of the systems with a strong screening between the fingers, present also, e.g., in side-branches growth in crystallization.²⁴ The deterministic character of the dynamics makes this system a perfect testing ground for the simplified models of finger growth. One of such models has been proposed in Ref. 17. It focuses on the thin-finger (large D and S) regime and approximates the fingers by thin lines growing at their tips only and interacting through the Laplacian pressure field. By the use of conformal mapping techniques, one can then predict the evolution of the fingering pattern in an accurate and fast way. We reiterate, however, that for these models to predict the final patterns, they first need to be fed with initial data obtained from the experiment and corresponding to the point in time when the noise ceases to affect the dynamics in a significant way.

The competition between the fingers is further demonstrated in Fig. 10, which shows the lengths and velocities of the winning finger (finger no. 35) together with its nearest neighbour (36) and second-nearest neighbour (37). The competition process is well visible here, with finger 36 being screened off first, and essentially stalled in its growth. On the other hand, fingers 35 and 37 continue to grow hand in hand, with very similar velocities, up to the point when their length becomes comparable with the distance between them (at $t \approx 0.5$ s), at which moment the longer finger begins to screen off the shorter one, hindering its growth.

The experimental data in Fig. 3 are in a good agreement with the numerical results (represented by the curves in Figure 10) up to the point where the longest finger covers about 80% of the length of the system. For the last stages of the evolution, near the breakthrough of the longest finger, the experimental finger seems to accelerate less than the one in the simulations. A possible reason for this might be the inability of our experimental setup to keep the pressure drop constant when the hydrodynamic resistance of our system is drastically decreased at the moment of breakthrough.

Next, we move to the analysis of the dependence of the finger patterns on the lattice parameters. The patterns obtained numerically for the immiscible fluids and different D and S values are presented in Fig. 11. In these calculations, to eliminate edge effects, periodic boundary conditions were applied along the transverse direction.

The parameters D and S affect the patterns in a different way. The former controls the width of the fingers: large value of D implies that the time it takes for the finger tip to cross a single

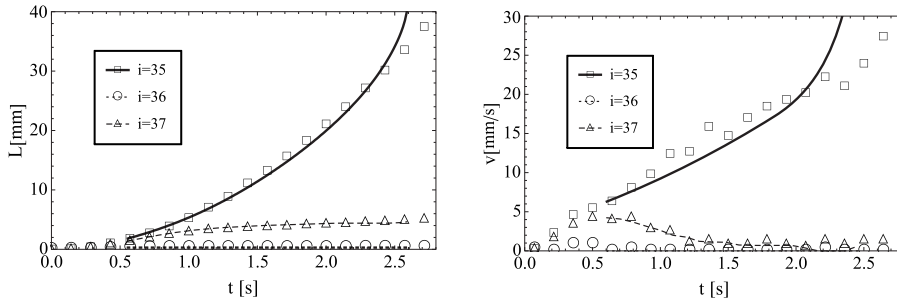


FIG. 10. Evolution of immiscible viscous fingers: lengths and velocities of the winning finger and its two neighbours. Measurements were made for fingers 35, 36, and 37 of Fig. 3 (counting from the left). The experimental data are shown by symbols, simulation results are represented by curves (corresponding to $t > 0.5$ s only, since the simulation was seeded with experimental results at $t = 0.5$ s).

longitudinal channel is shorter than that required to fill the transverse side channels, hence the finger tends to be thin in this regime. For $D > 2$, the width of the fingers is essentially reduced to a single transverse channel. This type of a finger has a distinct spear-like head, the shape of which is preserved during its growth. On the other hand, for smaller D , the fingers are significantly thicker, spanning several parallel channels.

Similar to what is observed in the experiment, the thick fingers appearing at small D show characteristic modulations along the axis. Their appearance can be understood by examining in more detail the dynamics of the invading fluid as it enters successive nodes. As shown in Fig. 12, once the finger tip enters a node (A), two side fingers begin to grow symmetrically in the perpendicular direction. Then, these fingers develop side branches themselves, which move downwards and compete with the main branch, so that the speed of the main finger drops. As a result, the side-branching in the next intersection (B) is less pronounced than in the previous one. Such a limited redistribution of

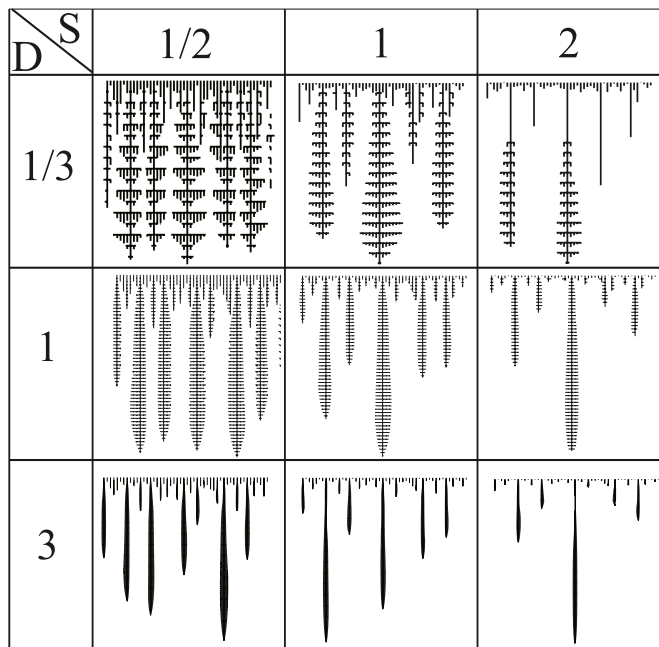


FIG. 11. Phase diagram of immiscible viscous fingering patterns for different values of D and S . The number of transverse channels is fixed in each system, $N_x = 50$; whereas the number of longitudinal channels $N_y = N_x D$, so that the physical size is kept constant in each case. Frames correspond to the moment when the longest finger reaches the end of the system.

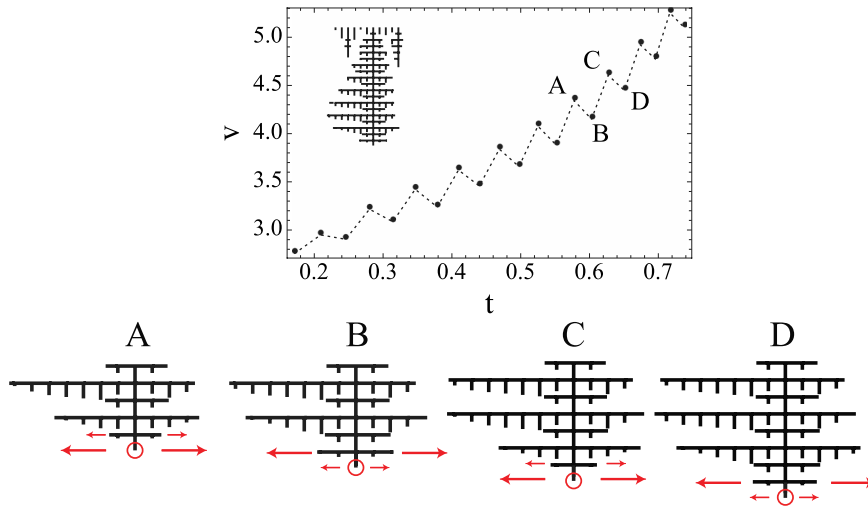


FIG. 12. Velocity of growing finger tip entering consecutive nodes ($D = 1/3$, $S = 1/2$). The time is scaled by the breakthrough time, whereas the velocity is scaled by the initial velocity of the invading fluid.

the flow to the perpendicular channels allows the flow in the main channel to increase again (C) and then the whole process repeats, producing a characteristic alternating pattern along the finger axis.

Returning to the analysis of the phase diagram, let us now discuss the impact of the cross section ratio, S , on the pattern. An inspection of Fig. 11 reveals that S governs the strength of interactions between the fingers. It is due to the fact that S determines the relative resistance of transverse channels ($R \sim \frac{D}{S^2}$). For small S , the resistance of the channels is large and the interaction is rather weak—nearly all fingers are of the same length. At larger S , the selection between the fingers becomes stronger, with the longer ones screening the shorter ones, preventing their growth. This leads to the appearance of a hierarchical, self-similar finger structure. The value of D has an opposite but less pronounced effect on the strength of interactions—with the increase of D the competition becomes more intense. The relative resistance plays then a similar role to that of diffusion length in side-branches growth in crystallization.²⁴

The analogous phase diagram for the miscible finger patterns is presented in Fig. 13. In this case, the viscosity ratio of 100 has been chosen in accordance with the experimental conditions.

The similarities between the miscible and immiscible case are connected with the fact that both the capillary number (for immiscible case) and particularly the Péclet number (for miscible case) have relatively large values, thus diffusive and capillary effects are of a lesser importance here. However, there are also differences between the immiscible and miscible case. First of all, as already mentioned in Sec. II, the significant new feature of the miscible patterns is the fact that the heads of the fingers become disconnected from their roots by the displaced fluid. This is fundamentally different from the snap-off phenomenon observed in the imbibition, which is due to the local fluctuations in the capillary pressure around a constriction in the pore. In our case, it is the invading fluid which is being snapped off and the mechanism is due to the interactions between the advancing fingers, analyzed in detail in Section VI.

The second difference between the immiscible and miscible case is the lack of modulations along the axes of the fingers—the side branches join with each other to form a uniform finger body in the absence of the surface tension preventing such a coalescence.

The lattice sizes in Figs. 11 and 13 were chosen in such a way as to guarantee the same physical size in each system: the number of transverse channels has been fixed ($N_x = 50$), whereas the number of longitudinal channels $N_y = N_x D$, so that L_x/L_y is constant in each case. This means, however, that the lattices used to model particular systems significantly differ in node numbers: from 50×17 (for $D = 1/3$) to 50×150 (for $D = 3$). One can thus wonder whether this can have an impact on the patterns—perhaps the small D patterns simply represent early stages of the displacement process, whereas large D patterns represent more developed flows? To elucidate

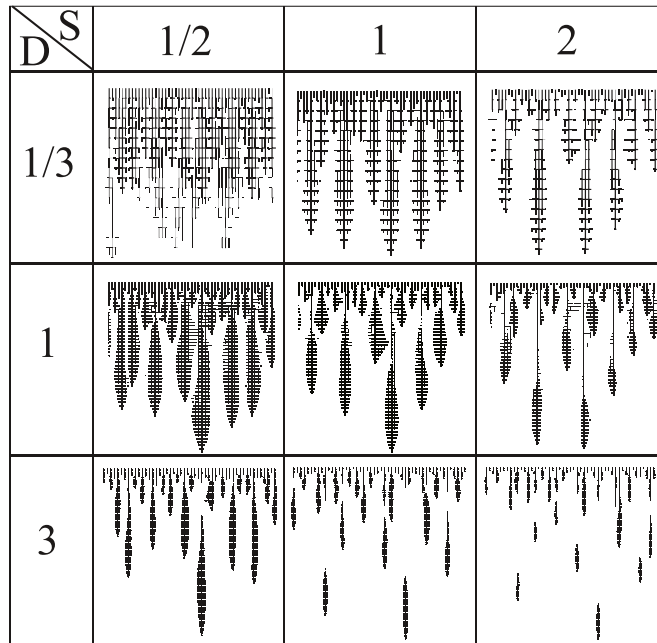


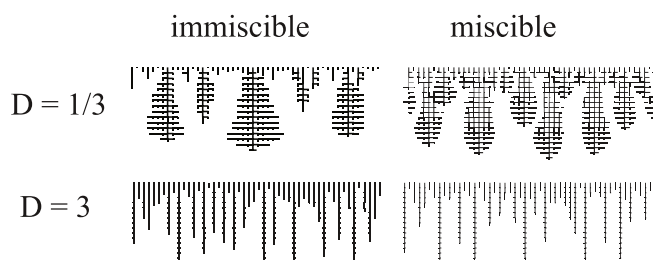
FIG. 13. Same as in Fig. 11 but for the miscible fluids.

that we present the finger pattern for $D = 1/2$ and $D = 3$, calculated in the same network (50×17 channels), captured at the moment when the length of the longest finger (measured in the number of longitudinal channels) coincides in both cases (Fig. 14). As it is observed, the qualitative difference between the patterns is still present. Apparently, the width of fingers (measured in the number of spanning channels) stabilizes in the early stages of system's evolution.

Finally, a note of caution should be added as to the generality of the phase diagrams discussed above. As already stated, the viscosity ratios and capillary number in these simulations have been set at the experimental values. Although we have not explored in detail the influence of these parameters on the phase diagrams, a series of runs at different μ_1/μ_2 and Ca values have suggested that this picture remains qualitatively correct, as long as we keep viscosity ratio and capillary number relatively large.

V. DISTRIBUTION OF FINGER LENGTHS

As already mentioned in the Introduction, the rectangular geometry of the system promotes competition between the fingers. When the lengths of the fingers become comparable to the distance between them, the fingers begin to screen each other off. As a result, approximately half of them are arrested in their growth, whereas the other half continues to grow. The process then repeats itself, leading to the appearance of the hierarchical growth pattern, as illustrated in Fig. 15. As noted by

FIG. 14. Comparison of the patterns for $D = 1/3$ and $D = 3$ produced on 50×17 lattice ($N_x = 50$, $N_y = 17$, $S = 1$). The same aspect ratio ($l_x/l_y = 1/3$) has been used for plotting all four pictures.

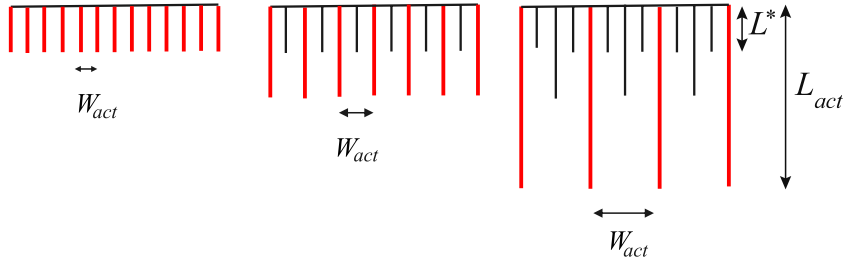


FIG. 15. Hierarchical growth of the fingers:^{52,53} initially many small fingers are formed (left panel), but due to the competition between them after a while only about a half of them continue to grow while the rest is screened (center panel). The process then repeats itself, leading to the appearance of a scale-invariant, power-law distribution of finger lengths. The active (growing) fingers are marked in red. Note that the characteristic distance between them, W_{act} , increases with time.

Huang *et al.*,⁵² the nature of the instability leading to appearance of the hierarchical pattern is the same as the initial Saffman-Taylor instability: the pressure gradient over the longer structures is larger than over the shorter ones (“lightning rod effect”). In time, the characteristic length between active (growing) fingers increases, while their number decreases, which results in a scale-invariant, power-law distribution of finger lengths,

$$N(L_f) \sim L_f^{-\alpha}, \quad (8)$$

where N denotes a number of fingers longer than L_f . An example distribution of the finger lengths obtained for $S = 1$, $D = 3$ (corresponding to plate 1) is shown in Fig. 16. As it is seen, the distribution indeed follows a power law with the exponent $\alpha \approx 1.1 - 1.2$, which is in agreement with the values reported in Ref. 53 for the hierarchical growth in dissolving rock. However, relatively large errors of the data together with relatively short span over which the power law is observed (less than a decade) do not allow us to exclude the possibility that the underlying power law is simply $N(L_f) \sim L_f^{-1}$, in agreement with the simple analytical models of 2d needle growth.⁵⁴ Note that in making the fit, we discarded the fingers shorter than $0.04L_y$ and longer than $0.45L_y$ (with L_y the system length): the former because their lengths are influenced by the lattice discretization effects, and the latter because the longest fingers remain active and the selection process there has not yet been concluded. The experimental results are averaged over five experimental runs, whereas the numerical data are averaged over 10 realizations of the noise on the 100×100 lattice.

Due to the quasi-2d geometry of the system, the competition between the fingers can be conveniently analyzed using conformal mapping techniques. This approach has been taken in Refs. 17 and 18 and yielded a number of insights on the finger-finger interaction. In particular, it has been shown¹⁸ that as soon as the fingers are allowed to capture the flow from one another, the fixed point appears in the phase space characterizing their dynamics, corresponding to the asymptotic state in which the growth of one of the fingers is hindered by the other.

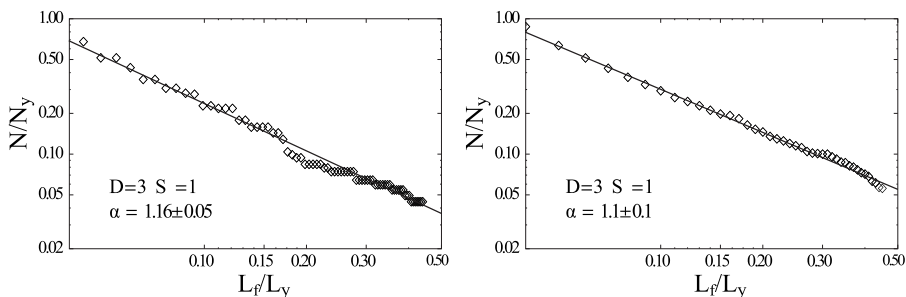


FIG. 16. Distribution of finger lengths obtained in experiment (left) and simulation (right) for immiscible fluid displacement on plate 1 ($D = 3$, $S = 1$). Fingers shorter than $0.04L_y$ and longer than $0.45L_y$ (with L_y the system length) were not taken into account in the distribution. The solid line corresponds to the fit $N(L_f) \sim L_f^{-\alpha}$.

Here we focus on the influence of the network geometry on the competition between the fingers. To this end, we analyze the dependence of the length of the shortest fingers in the system, L^* , on the network characteristics. Since these fingers have already been screened off, they no longer grow and—at least in the limit of infinite viscosity ratio—they remain “frozen” at the length, L^* , which they had at the moment when they have lost the competition. The larger L^* , the weaker the competition in the system. To analyze quantitatively the dependence of L^* on the lattice parameters, let us note first that within a single phase (e.g., the displaced one) Equations (1) and (2) can be viewed as the discretization of the anisotropic Laplace equation,⁵⁵

$$s_x^2 l_x \frac{\partial^2 p}{\partial^2 x} + s_y^2 l_y \frac{\partial^2 p}{\partial^2 y} = 0. \quad (9)$$

By rescaling the coordinates by

$$x' = \frac{l_0}{l_x} x, \quad y' = \frac{l_0}{\sqrt{l_y l_x}} \frac{s_x}{s_y} y, \quad (10)$$

we can map different lattices onto a single “master” system (see Fig. 17), which is described by a standard Laplace equation for the pressure outside the fingers in (x', y') coordinates. The length of the horizontal channels in this system is equal to l_0 .

The patterns produced in the course of the evolution of the master system can then be mapped back onto the original lattices. In particular, the finger length in the original lattice, L^* , is then linked with that in the master system, L_m^* , by

$$L^* = \frac{\sqrt{l_y l_x} s_y}{l_0 s_x} L_m^*. \quad (11)$$

Or, if we measure the length of the shortest fingers in terms of how many vertical channels they cover,

$$\tilde{L}^* \equiv \frac{L^*}{l_y} \sim \frac{\sqrt{D}}{S}. \quad (12)$$

This scaling can be checked against the simulation results. Fig. 18 shows the analysis of the dependence of the length of the shortest channels on D and S based on the numerical data. In each panel, one of these parameters has been varied whilst the other kept fixed. Our procedure of collecting the lengths of the shortest fingers was based on the observation that the shortest fingers are always the neighbours of the longest ones (cf. Fig. 15). We have proceeded as follows: at the moment when the longest finger has reached the end of the system, we have identified all fingers longer than $2/3$ of the system, and then have taken the average of the lengths of their neighbours, identifying this with L^* .

The first panel of Fig. 18 presents the fit to $\tilde{L}^*(D)$ dependence for $S = 1$ and $\mu_2/\mu_1 = 100$, with the line marking the theoretical $(D^{1/2})$ slope. As observed, the agreement with theory is better for

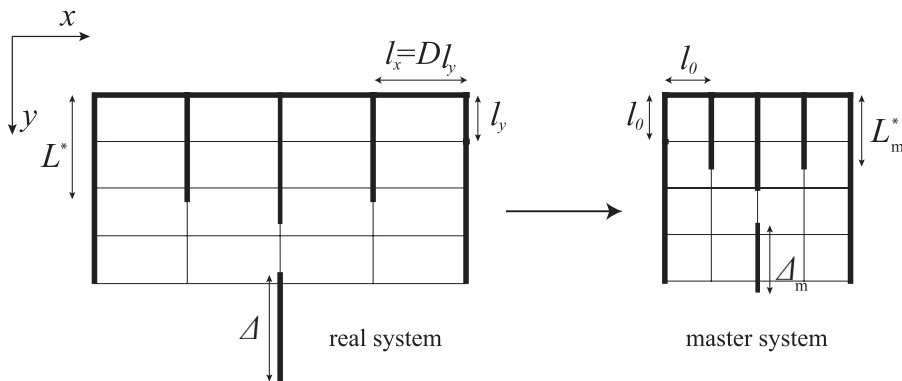


FIG. 17. Mapping of different lattices onto a single “master” system.

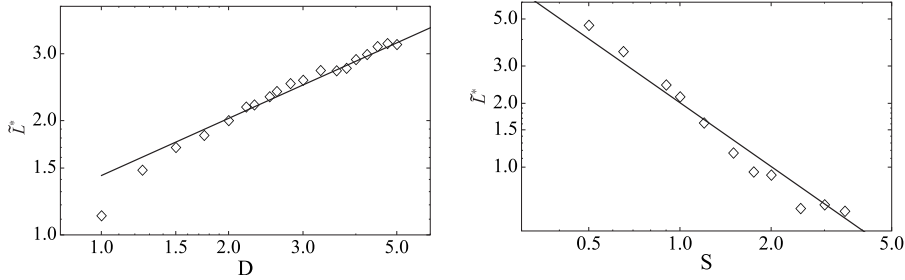


FIG. 18. The length of the shortest fingers in the system \tilde{L}^* as a function of D and S for simulations with immiscible fluids. Left: $\tilde{L}^*(D)$ for $S = 1$ together with the $D^{1/2}$ curve (solid line). Right: \tilde{L}^* at $D = 3$ as a function of S together with the $1/S$ curve (solid line).

large values of D , corresponding to the thin-finger regime, where the growth is indeed hierarchical and the competition between the fingers is strong. The right panel of Fig. 18 shows the fit to the $\tilde{L}^*(S)$ dependence at $D = 3$ and again $\mu_1/\mu_2 = 100$. The theoretical slope (S^{-1}) is in a good agreement with these data.

The estimates of L^* allow one also to obtain the dependence between the width of the active region, W_{act} , and the length the active fingers. Namely, let us assume an inverse linear distribution of finger lengths

$$N(L_f) = \frac{\kappa}{L_f}, \quad (13)$$

which is a good approximation to the distributions reported above. Then, considering the distribution of finger lengths in a single hierarchical cell (a part of the system of width W_{act} , cf. Fig. 15), we get on one hand

$$1 = \frac{\kappa}{L_{act}} \quad (14)$$

and on the other

$$N_{tot} = \frac{\kappa}{L^*}, \quad (15)$$

where N_{tot} is the total number of channels in the elementary cell. The above relations combined imply that

$$\frac{W_{act}}{l_x} = N_{tot} = \frac{L_{act}}{L^*}, \quad (16)$$

so that the aspect ratio of the single hierarchical cell is

$$\frac{L_{act}}{W_{act}} = \tilde{L}^* \frac{l_y}{l_x} \sim \frac{1}{\sqrt{DS}}, \quad (17)$$

which is in agreement with the features of the phase diagram in Fig. 11. As observed, the active region is the widest in the lower right corner of the diagram (i.e., for large D and S) and then its width decreases both with S and with D . However, one should keep in mind that the above reasoning holds in principle only in the hierarchical growth regime, where the distribution of the finger lengths obeys (13), i.e., for both D and S larger than 1.

VI. MISCIBLE DROP FORMATION

In this section, we look more closely at the process of tearing off the fingers' heads which leads to the miscible drop formation. The analysis of experimental and numerical data shows that the drops are surprisingly stable, preserving their lengths and shapes in the course of the evolution. Over the period between the tear-off and the time when they reach the outlet, their lengths change

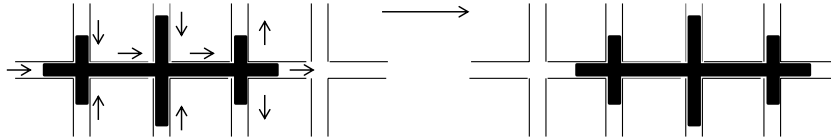


FIG. 19. A schematic of the motion of water in the channel network needed in order for a translation of a drop.

by 5%–10% only. Korteweg stresses have been proposed to act as a factor stabilizing the miscible drops.⁵⁶ In the present system, however, they do not seem to play a deciding role: the shapes of the drops, their motion, and stability are well predicted by the numerical model described in Sec. III, which does not take the Korteweg stresses into account. The permanence of the shape of the drops is rather remarkable, given that, due to the presence of the underlying lattice, the drop cannot move through the system by a simple translation. Instead, as illustrated schematically in Fig. 19, water needs to be constantly pushed out of the capillaries at the rear of the drop and into those at the front in a highly coordinated manner so that the overall shape of the inclusion remains the same. The flow lines suggest that the flow around the head is a combination of the doublet and uniform flow, similar to the flow patterns in a translating bubble in a Hele-Shaw cell, as calculated by Taylor and Saffman.⁵⁷

The inspection of Fig. 13 reveals that the length of a miscible drop depends on the lattice characteristics: for larger S and D , the drops tend to be shorter and the tearing off takes place earlier. An insight into the exact mechanism by which the heads of the fingers become disconnected can be gained by analyzing the flow of the invading and displaced fluid in between the growing fingers. Fig. 20 presents the flow patterns in the vicinity of a longer finger flanked by two shorter ones. A characteristic “converging-diverging” pattern is observed there, with the flow directed towards the longer channel in the upstream part and outwards from the main channel in the downstream part. The origin of such a pattern can be elucidated by analyzing the pressure drops in the fingers, as shown schematically in Fig. 21. Since there is a constant pressure drop between the inlet and outlet, the pressure gradient in the longer finger will be steeper than in the shorter one; this is because the flow rate is higher in the long finger. In the upstream part of the system, the short finger is at a higher pressure than the long one, so the flow is directed toward the long finger. Downstream, the region around the tip of the long finger is at a higher pressure than the surrounding network, hence the flow is directed away from the finger, resulting in the flow pattern observed in Fig. 20. Such a “converging-diverging” flow pattern is a characteristic feature of the fingered growth systems, also observed in the growth of dissolution channels in porous rock.^{20,58}

The large pressure gradient between the tip of the shorter finger and the body of the longer one causes a strong flow of displaced fluid toward the longer finger, which cuts off most of the

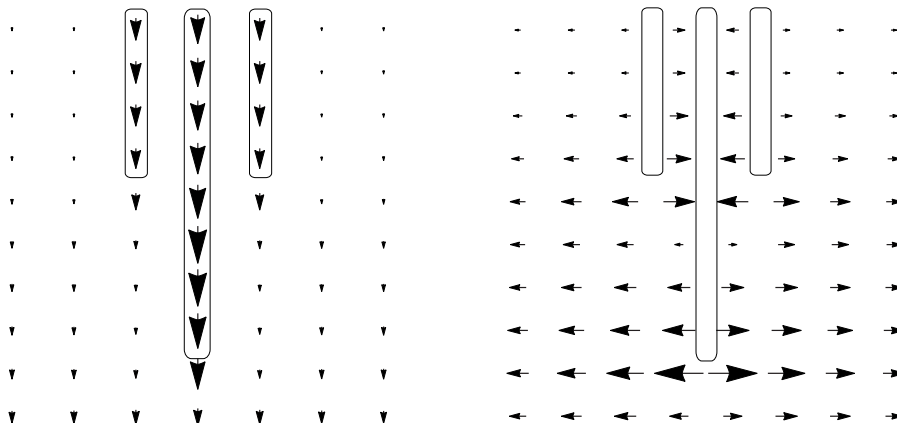


FIG. 20. The flow around a longer finger (in the center) flanked by the two shorter ones. The panels on the left show the flow in the longitudinal channels, the panels on the right—in the transverse ones.

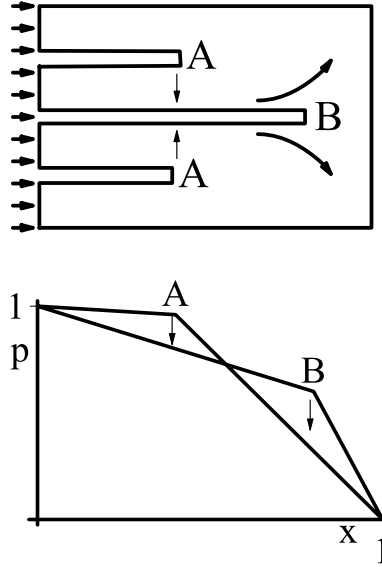


FIG. 21. A long finger with the two shorter neighbors and the corresponding pressure drops. The flow lines are converging towards a longer finger at the inlet and diverging near the tip of the finger.

flow of the invading fluid. As a result, the finger head becomes almost disconnected from the body except for a small thread of an invading liquid (which can be discerned upon careful examination of experimental patterns and is also present in the simulation results).

The dependence of the drop length on the lattice parameters can be assessed along the similar lines as in Sec. V. Again—using transformation (10)—we map the systems characterized by particular D and S onto a master system, in which the pressure in the displaced phase is described by an isotropic Laplace equation. The length of the drops in the original lattice, Δ , is then linked with that in the master system, Δ_m (see Fig. 17), by

$$\tilde{\Delta} \equiv \frac{\Delta}{l_y} = \sqrt{\frac{l_x s_y \Delta_m}{l_y s_x l_0}} \sim \frac{\sqrt{D}}{S}, \quad (18)$$

where $\tilde{\Delta}$ is a characteristic length of the drop (measured in terms of how many longitudinal channels it covers) whereas Δ_m is the length of the drop in the master system.

This scaling is checked against simulation results in Fig. 22. The left panel of this figure shows $\tilde{\Delta}S$ as a function of D for three different S values at $\mu_1/\mu_2 = 100$. According to (18), these dependences should scale as $D^{1/2}$, and this is indeed observed in the range of intermediate and large D , where the data points of different S overlap and approach the $D^{1/2}$ curve (solid line). As already

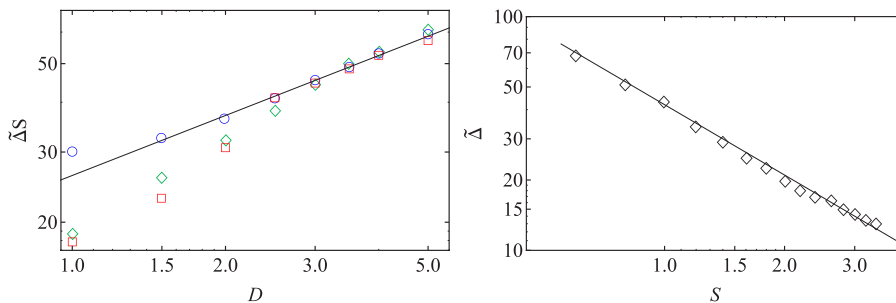


FIG. 22. The average drop length $\tilde{\Delta}$ as a function of D and S for simulations with miscible fluids. Left: $\tilde{\Delta}S(D)$ for three different values of S : $S = 1/2$ (squares), $S = 1$ (diamonds), and $S = 2$ (circles) together with the $D^{1/2}$ curve (solid line). Right: $\tilde{\Delta}$ at $D = 3$ as a function of S together with the $1/S$ curve (solid line).

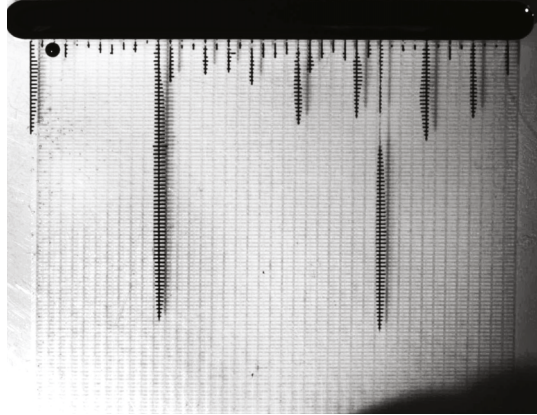


FIG. 23. Droplet formation in experiment on plate no. 1 with immiscible fluids (water infiltrating oil).

noted in Sec. V, for smaller D , the pattern ceases to be hierarchical and scalings no longer hold. The next panel of Fig. 22 shows the $\Delta \sim (S)$ dependence at $D = 3$ and again $\mu_1/\mu_2 = 100$. A linear decrease is observed here, as predicted by (18).

We conclude with two comments. First, tearing off of the finger heads could in principle take place also in the immiscible case, if only the viscous pressure drop in the inlet region (driving the displaced liquid towards the longer fingers) is sufficiently large in comparison to the capillary pressure. Such large pressure gradients will break the liquid filament in the main channel and lead to the drop formation. Indeed, as shown in Fig. 23, we have observed such a behaviour in the experiments on plate 1 after increasing the pressure drop by a factor of two with respect to that used in the experiments of Figs. 3-6.

Finally, a similar phenomenon of “miscible drop” formation has also been reported in the numerical simulations of De Wit and Homsy⁵⁹ and in the simulations of Chen *et al.*,⁶⁰ however, in a somewhat different physical context, De Wit and Homsy⁵⁹ have analyzed viscous fingering coupled with chemical reactions; in this case, the drop formation was related to the bistable character of the reaction kinetics. On the other hand, in Ref. 60 the formation of the droplets was observed in simulations of miscible fingering in lifting Hele-Shaw cell.

VII. SUMMARY

In this paper, we have studied experimentally and numerically viscous fingering in a rectangular network of microfluidic channels. Depending on the network geometry, a variety of different patterns have been observed, ranging from the thick fingers, spanning several lattice spacings to the long-and-thin structures involving essentially a single channel. The latter were of a particular interest to us, due to their appearance in variety of other pattern forming systems in nature. We have studied the interaction between the fingers, leading to the appearance of a hierarchical, scale-free growth pattern. In the thin-finger regime, the simulations show a remarkable agreement with the experimental data on the finger evolution, which is a reflection of the deterministic character of the dynamics. The fingers are well-separated and not merging together, and the interaction between them is mediated through the pressure field only. This makes the present system particularly suitable for testing different approximate models of finger growth. Interestingly, strong lateral pressure gradients in the vicinity of the longest fingers can lead to the disconnection of the heads of the fingers from their bases, which arrests their further growth. This phenomenon is particularly pronounced in the miscible case, since the surface tension will tend to stabilize the filament of the invading fluid. The miscible drops, formed as a result of a pinch-off of fingers heads, continue to move through the system, preserving their shapes. They have a well-defined length, which depends on the geometry of the lattice.

ACKNOWLEDGMENTS

This work was supported by the National Science Centre (Poland) under research Grant No. 2012/07/E/ST3/01734 (to P.S.) and in part by the Foundation for Polish Science Team Programme co-financed by the EU European Regional Development Fund (No. 2010-6/2 for A.B. and No. 2008-1/1 for P.G. and A.S.), co-financed within the European Research Council Starting Grant 279647 (to P.G.). We also thank The European Regional Development Fund under the Operational Programme Innovative Economy NanoFun POIG.02.02.00-00-025/09 for supporting part of the research infrastructure.

- ¹ S. Hill, "Channeling in packed columns," *Chem. Eng. Sci.* **1**, 247–253 (1952).
- ² P. G. Saffman and G. Taylor, "The penetration of a fluid into a porous medium or Hele-Shaw cell containing a more viscous liquid," *Proc. R. Soc. A* **245**, 312–329 (1958).
- ³ R. A. Wooding, "Growth of fingers at an unstable diffusing interface in a porous medium or Hele-Shaw cell," *J. Fluid Mech.* **39**, 477–495 (1969).
- ⁴ L. Paterson, "Radial fingering in a Hele Shaw cell," *J. Fluid Mech.* **113**, 513–529 (1981).
- ⁵ G. M. Homsy, "Viscous fingering in porous media," *Annu. Rev. Fluid Mech.* **19**, 271–311 (1987).
- ⁶ R. L. Chuoke, P. Van Meurs, and C. Van der Poel, "The instability of slow, immiscible, viscous liquid–liquid displacement in permeable media," *Trans. AIME* **216**, 188–194 (1959).
- ⁷ J. P. Stokes, D. A. Weitz, J. P. Gollub, A. Dougherty, M. O. Robbins, P. M. Chaikin, and H. M. Lindsay, "Interfacial stability of immiscible displacement in a porous medium," *Phys. Rev. Lett.* **57**, 1718 (1986).
- ⁸ G. Løvøll, Y. Méheust, R. Toussaint, J. Schmittbuhl, and K. J. Måløy, "Growth activity during fingering in a porous Hele–Shaw cell," *Phys. Rev. E* **70**, 026301 (2004).
- ⁹ T. Vicsek, *Fractal Growth Phenomena* (World Scientific, Singapore, 1989).
- ¹⁰ P. Meakin, *Fractals, Scaling and Growth Far from Equilibrium* (Cambridge University Press, Cambridge, 1998).
- ¹¹ J.-D. Chen and D. Wilkinson, "Pore-scale viscous fingering in porous media," *Phys. Rev. Lett.* **55**, 1892–1895 (1985).
- ¹² E. Ben-Jacob, R. Godbey, N. D. Goldenfeld, J. Koplik, H. Levine, T. Mueller, and L. M. Sander, "Experimental demonstration of the role of anisotropy in interfacial pattern formation," *Phys. Rev. Lett.* **55**, 1315–1318 (1985).
- ¹³ J.-D. Chen, "Radial viscous fingering patterns in Hele-Shaw cells," *Exp. Fluids* **5**, 363–371 (1987).
- ¹⁴ V. Horváth, T. Vicsek, and J. Kertész, "Viscous fingering with imposed uniaxial anisotropy," *Phys. Rev. A* **35**, 2353–2356 (1987).
- ¹⁵ L. Carleson and N. Makarov, "Laplacian path models," *J. Anal. Math.* **87**, 103 (2002).
- ¹⁶ T. Gubiec and P. Szymczak, "Fingered growth in channel geometry: A Loewner-equation approach," *Phys. Rev. E* **77**, 041602 (2008).
- ¹⁷ M. Pecelerowicz, A. Budek, and P. Szymczak, "Effective description of the interaction between anisotropic viscous fingers," *EPL* **108**, 14001 (2014).
- ¹⁸ M. Pecelerowicz, A. Budek, and P. Szymczak, "Competition between anisotropic viscous fingers," *Eur. Phys. J. Spec. Top.* **223**, 1895–1906 (2014).
- ¹⁹ A. Kuhn and F. Argoul, "Spatiotemporal morphological transitions in thin-layer electrodeposition: The Hecker effect," *Phys. Rev. E* **49**, 4298–4305 (1994).
- ²⁰ P. Szymczak and A. J. C. Ladd, "Wormhole formation in dissolving fractures," *J. Geophys. Res.* **114**, B06203, doi:10.1029/2008jb006122 (2009).
- ²¹ O. Zik, Z. Olami, and E. Moses, "Fingering instability in combustion," *Phys. Rev. Lett.* **81**, 3868–3871 (1998).
- ²² O. Zik and E. Moses, "Fingering instability in combustion: An extended view," *Phys. Rev. E* **60**, 518–531 (1999).
- ²³ Y. Couder, F. Argoul, A. Arnéodo, J. Maurer, and M. Rabaud, "Statistical properties of fractal dendrites and anisotropic diffusion-limited aggregates," *Phys. Rev. A* **42**, 3499–3503 (1990).
- ²⁴ Y. Couder, J. Maurer, R. González-Cinca, and A. Hernández-Machado, "Side-branch growth in two-dimensional dendrites. I. Experiments," *Phys. Rev. E* **71**, 31602 (2005).
- ²⁵ O. Devauchelle, A. P. Petroff, H. F. Seybold, and D. H. Rothman, "Ramification of stream networks," *Proc. Natl. Acad. Sci. U. S. A.* **109**, 20832–20836 (2012).
- ²⁶ A. P. Petroff, O. Devauchelle, H. Seybold, and D. H. Rothman, "Bifurcation dynamics of natural drainage networks," *Philos. Trans. R. Soc., A* **371**, 20120365 (2013).
- ²⁷ M. Blunt, M. J. King, and H. Scher, "Simulation and theory of two-phase flow in porous media," *Phys. Rev. A* **46**, 7680 (1992).
- ²⁸ E. Aker, K. J. Måløy, A. Hansen, and G. G. Batrouni, "A two-dimensional network simulator for two-phase flow in porous media," *Transp. Porous Media* **32**, 163–186 (1998).
- ²⁹ P. Van Meurs, "The use of transparent three-dimensional models for studying the mechanism of flow processes in oil reservoirs," *Trans. AIME* **210**, 295–301 (1957).
- ³⁰ R. Lenormand, C. Zarccone, and A. Sarr, "Mechanisms of the displacement of one fluid by another in a network of capillary ducts," *J. Fluid Mech.* **135**, 337–353 (1983).
- ³¹ R. Lenormand and C. Zarccone, "Two-phase flow experiments in a two-dimensional medium," *Phys. Chem. Hydrodyn.* **6**, 497–506 (1985).
- ³² R. Lenormand, "Différents mécanismes de déplacements visqueux et capillaires en milieu poreux: Diagramme de phase," *C. R. Acad. Sci. Paris II* **301**, 247–250 (1985).
- ³³ K. J. Måløy, F. Boger, J. Feder, and T. Jøssang, "Dynamics and structure of viscous fingers in porous media," in *Time-Dependent Effects in Disordered Materials* (Springer, 1987), pp. 111–138.

- ³⁴ K. J. Måløy, F. Boger, J. Feder, T. Jøssang, and P. Meakin, "Dynamics of viscous-fingering fractals in porous media," *Phys. Rev. A* **36**, 318 (1987).
- ³⁵ R. Lenormand, E. Touboul, and C. Zarcone, "Numerical models and experiments on immiscible displacements in porous media," *J. Fluid Mech.* **189**, 165–187 (1988).
- ³⁶ R. Lenormand, "Flow through porous media: Limits of fractal patterns," *Proc. R. Soc. A* **423**, 159–168 (1989).
- ³⁷ J.-D. Chen and J. Koplik, "Immiscible fluid displacement in small networks," *J. Colloid Interface Sci.* **108**, 304–330 (1984).
- ³⁸ W. E. Soll, M. A. Celia, and J. L. Wilson, "Micro-model studies of three-fluid porous media systems: Pore-scale processes relating to capillary pressure-saturation relationships," *Water Resour. Res.* **29**, 2963–2974, doi:10.1029/93WR00524 (1993).
- ³⁹ J.-T. Cheng, J. P. Morris, J. Tran, A. Lumsdaine, N. J. Giordano, D. D. Nolte, and L. J. Pyrak-Nolte, "Single-phase flow in a rock fracture: Micro-model experiments and network flow simulation," *Int. J. Rock Mech. Min. Sci.* **41**, 687–693 (2004).
- ⁴⁰ H. Ovdal and B. Berkowitz, "Pore-scale study of drainage displacement under combined capillary and gravity effects in index-matched porous media," *Water Resour. Res.* **42**, W06411, doi:10.1029/2005wr004553 (2006).
- ⁴¹ M. Wu, F. Xiao, R. M. Johnson-Pabon, S. T. Retterer, X. Yin, and K. B. Neeves, "Single-and two-phase flow in microfluidic porous media analogs based on Voronoi tessellation," *Lab Chip* **12**, 253–261 (2012).
- ⁴² W. De Malsche, J. Op De Beeck, H. Gardeniers, and G. Desmet, "Visualization and quantification of the onset and the extent of viscous fingering in micro-pillar array columns," *J. Chromatogr. A* **1216**, 5511–5517 (2009).
- ⁴³ C. Cottin, H. Bodiguel, and A. Colin, "Influence of wetting conditions on drainage in porous media: A microfluidic study," *Phys. Rev. E* **84**, 026311 (2011).
- ⁴⁴ W. Xu, J. T. Ok, F. Xiao, K. B. Neeves, and X. Yin, "Effect of pore geometry and interfacial tension on water-oil displacement efficiency in oil-wet microfluidic porous media analogs," *Phys. Fluids* **26**, 093102 (2014).
- ⁴⁵ D. Ogonczyk, J. Węgrzyn, P. Jankowski, B. Dabrowski, and P. Garstecki, "Bonding of microfluidic devices fabricated in polycarbonate," *Lab Chip* **10**, 1324–1327 (2010).
- ⁴⁶ J.-D. Chen, "Pore-scale difference between miscible and immiscible viscous fingering in porous media," *AIChE J.* **33**, 307–311 (1987).
- ⁴⁷ P. Petitjeans and T. Maxworthy, "Miscible displacements in capillary tubes. Part 1. Experiments," *J. Fluid Mech.* **326**, 37–56 (2006).
- ⁴⁸ C.-Y. Chen and E. Meiburg, "Miscible displacements in capillary tubes. Part 2. Numerical simulations," *J. Fluid Mech.* **326**, 57–90 (1996).
- ⁴⁹ P. R. Amestoy, I. S. Duff, J. Koster, and J.-Y. L'Excellent, "A fully asynchronous multifrontal solver using distributed dynamic scheduling," *SIAM J. Matrix Anal. Appl.* **23**, 15–41 (2001).
- ⁵⁰ P. R. Amestoy, A. Guermouche, J.-Y. L'Excellent, and S. Pralet, "Hybrid scheduling for the parallel solution of linear systems," *Parallel Comput.* **32**, 136–156 (2006).
- ⁵¹ N. A. Mortensen, F. Okkels, and H. Bruus, "Reexamination of Hagen-Poiseuille flow: Shape dependence of the hydraulic resistance in microchannels," *Phys. Rev. E* **71**, 057301 (2005).
- ⁵² Y. Huang, G. Ouillon, H. Saleur, and D. Sornette, "Spontaneous generation of discrete scale invariance in growth models," *Phys. Rev. E* **55**, 6433 (1997).
- ⁵³ P. Szymczak and A. J. C. Ladd, "A network model of channel competition in fracture dissolution," *Geophys. Res. Lett.* **33**, L05401, doi:10.1029/2005GL025334 (2006).
- ⁵⁴ J. Krug, K. Kessner, P. Meakin, and F. Family, "Laplacian needle growth," *Europhys. Lett.* **24**, 527–532 (1993).
- ⁵⁵ J. K. Lin and D. G. Grier, "Stability of densely branched growth in dissipative diffusion-controlled systems," *Phys. Rev. E* **54**, 2690–2695 (1996).
- ⁵⁶ C.-Y. Chen, L. Wang, and E. Meiburg, "Miscible droplets in a porous medium and the effects of Korteweg stresses," *Phys. Fluids* **13**, 2447–2456 (2001).
- ⁵⁷ G. Taylor and P. G. Saffman, "A note on the motion of bubbles in a Hele–Shaw cell and porous medium," *Q. J. Mech. Appl. Math.* **12**, 265–279 (1959).
- ⁵⁸ P. Kelemen, J. Whitehead, E. Aharonov, and K. Jordahl, "Experiments on flow focusing in soluble porous media, with applications to melt extraction from the mantle," *J. Geophys. Res.* **100**(B1), 475–496, doi:10.1029/94JB02544 (1995).
- ⁵⁹ A. De Wit and G. M. Homsy, "Viscous fingering in reaction–diffusion systems," *J. Chem. Phys.* **110**, 8663–8675 (1999).
- ⁶⁰ C.-Y. Chen, C.-H. Chen, and J. A. Miranda, "Numerical study of miscible fingering in a time-dependent gap Hele–Shaw cell," *Phys. Rev. E* **71**, 056304 (2005).